AIAA JOURNAL
Vol. 51, No. 8, August 2013

Sidewall Boundary Layer of Transverse Waves in Simulated Liquid Rocket Engines

Charles T. Haddad* and Joseph Majdalani†
University of Tennessee Space Institute, Tullahoma, Tennessee 37388

DOI: 10.2514/1.J052260

This work seeks to provide a closed-form analytical solution for the transverse vortical wave generated at the sidewall of a circular cylinder with headwall injection. This particular configuration mimics the conditions leading to the onset of traveling radial and tangential waves in an idealized liquid rocket engine chamber. Assuming a short cylindrical enclosure with axisymmetric injection, regular perturbations are used to linearize the problem's conservation equations. Flow decomposition is subsequently applied to the first-order disturbance equations, thus giving rise to a compressible, inviscid, acoustic set responsible for driving the unsteady motion and to an incompressible, viscous, vortical set driven by virtue of coupling with the acoustic mode along both the sidewall and headwall. While the acoustic mode is readily recovered from the wave equation, the induced vortical mode is resolved using boundary-layer theory and an expansion of the rotational equations with respect to a small viscous parameter, δ. At the outset, an explicit formulation for the leading-order vortical field is derived and verified numerically. A radial penetration number akin to the Stokes or Womersley numbers is identified and found to control the penetration depth of the viscous boundary layer forming above the inert sidewall. This parameter is based on the transverse oscillation mode frequency and scales with the squared ratio of the Stokes layer and the chamber's characteristic radius.

Nomenclature

a_0	=	$(\gamma RT_0)^{1/2}$, speed of sound of incoming flow
L	=	chamber length
M_b	=	average blowing Mach number at the headwall
Pr	=	Prandtl number, ratio of kinematic viscosity to thermal diffusivity
p	=	pressure
R	=	chamber radius
Re_a	=	a_0R/ν_0, acoustic Reynolds number
Re_k	=	$\omega_{mn}R^2/\nu_0$, kinetic Reynolds number
r, θ, z	=	radial, tangential, and axial coordinates
S_r	=	radial penetration number
T	=	temperature
t	=	time
$\boldsymbol{U}$	=	mean flow velocity vector
$U_b(r)$	=	blowing velocity profile at the headwall
$\boldsymbol{u}$	=	total velocity vector
α	=	$R(\omega_{mn}/\nu_0)^{1/2}$, Womersley number
δ	=	$Re_a^{-1/2}$, viscous parameter
δ_d	=	$\delta(\eta_0/\mu_0 + 4/3)^{1/2}$, dilatational parameter
δ_{BL}	=	boundary-layer thickness
γ	=	ratio of specific heats
ε	=	wave amplitude
η	=	bulk viscosity
λ_S	=	$R\sqrt{\omega_{mn}/(2\nu_0)}$, Stokes number
μ	=	dynamic viscosity
ν	=	μ/ρ, kinematic viscosity
ρ	=	density
$\boldsymbol{\Omega}$	=	mean vorticity
$\boldsymbol{\omega}$	=	unsteady vorticity
ω_{mn}	=	a_0k_{mn}/R, circular frequency

Subscript

0	=	mean chamber properties

Superscripts

$*$	=	dimensional variables
$'$	=	unsteady flow variable
$-$	=	steady flow variable

Presented as Paper 2012-4086 at the 63rd AIAA Southeastern Regional Student Conference, Cape Canaveral, FL, 2–3 April 2012; received 5 August 2012; revision received 10 December 2012; accepted for publication 14 December 2012; published online 9 May 2013.

*Graduate Research Assistant; Department of Mechanical, Aerospace and Biomedical Engineering. Member AIAA.

†H. H. Arnold Chair of Excellence in Advanced Propulsion; Department of Mechanical, Aerospace and Biomedical Engineering. Associate Fellow AIAA.

I. Introduction

ACOUSTIC instability has long been viewed as a principal hurdle hampering the development of large-scale combustors, especially those intended for heavy lift and power generation. In fact, given the violent oscillations that instability mechanisms can engender, they have been universally recognized among the chief impediments resulting in the frequent cancellation of new rocket launch programs. Thus motivated by the need to predict and prevent the occurrence of these anomalies, a series of studies involving solid, liquid, and hybrid rockets has been carried out with the underlying theme of quantifying the various sources of instability. These have encompassed all three means of investigations, namely those based on experimental, numerical, and theoretical considerations.

Historically, some of the earliest analytical studies of oscillatory phenomena in cylindrical tubes with injecting walls may have been undertaken by Hart and McClure [1,2] and Culick [3,4]. These models led to several analytical approximations that could be used to describe the behavior of acoustic waves in porous chambers. Subsequent studies have emphasized the limitations of inviscid-irrotational models and emphasized the need to observe the no-slip requirement at the propellant surface [5–7]. For example, the classical experiments by Brown et al. [8] and Dunlap et al. [9] showed that irrotational models failed to reproduce the actual behavior directly above the propellant surface. Moreover, the computational-fluid-dynamics simulations of Vuillot and Avalon [10] predicted a thick boundary layer at the sidewall, specifically one that could extend over the majority of the chamber volume. Other

asymptotic investigations led to closed-form approximations of the vorticoacoustic waves and their penetration within a rocket motor, and these showed a strong dependence on the chamber's mean flow and acoustic modes [11–14].

Despite the variety of mathematical formulations devoted to the description of either mean [15–19] or oscillatory waves in solid rocket motor (SRM) internal flows [20–22], substantially fewer models seem to have tackled the liquid rocket engine (LRE) case [23–25]. Some exceptions may be found, and these may be identified in studies such as those by Flandro et al. [26,27] and Fischbach et al. [28]. The latter considers the transverse wave propagation problem in a simulated LRE with the aim of better understanding the mechanism of acoustic streaming. Assuming waves generated by uniform headwall injection, these researchers also analyze the vorticoacoustic boundary layer forming above the injector faceplate. Later studies by Haddad and Majdalani [29,30] introduce a framework for describing the transverse evolution of vorticoacoustic waves and their dependence on variable headwall injection patterns. However, despite the ability of their solutions to satisfy the no-slip requirement at the headwall and partially at the sidewall, their tangential motion still permits slippage along the sidewall. To overcome this technical deficiency, the main focus of the present study will be placed on a boundary-layer treatment of the sidewall.

In seeking to overcome the deficiency of former transverse wave models in the tangential direction, this sequel devotes itself to the asymptotic treatment of the tangential motion in the vicinity of the sidewall. To this end, the unsteady flowfield is considered in a short cylindrical chamber with a porous headwall that permits the injection of axisymmetric mean flow patterns. Then, following the small perturbation approach introduced by Chu and Kovásznay [31], the equations of motion are split into two sets that control the mean and unsteady flow components, respectively. Similarly, using the Helmholtz decomposition theorem, the first-order fluctuations are separated into a pair of acoustic and vortical fields. Presently, these techniques are used to derive an improved asymptotic solution for the oscillatory motion in a circular chamber in general, and a simulated LRE in particular. In fact, based on a systematic application of boundary-layer theory, a mathematical formulation will be achieved for the sidewall boundary layer, which complements our previous analysis of the headwall region. Through this effort, a more complete and accurate description of the vorticoacoustic waves in simulated LREs will be realized.

II. Formulation

A. Geometry

To simulate the unsteady motion in a liquid rocket engine, an idealized version of the latter must be conceived. The thrust chamber is thus modeled as a horizontal cylinder extending from $z^* = 0$ to L, with a small aspect ratio that is assumed to be less than or equal to unity. Radially, the domain extends from the centerline at $r^* = 0$ to the sidewall at $r^* = R$. In addition to schematically illustrating a right-cylindrical chamber with an injecting headwall, Fig. 1 shows the azimuthal coordinate θ and the transverse direction of unsteady velocity disturbances, u'_θ and u'_r, which define both tangential and radial oscillations.

B. Acoustic and Vortical Systems of Equations

A normalization of the governing equations is required to generalize the problem at hand and highlight the terms pertinent to our analysis. A nondimensional version of the conservation equations can be obtained by normalizing the flow variables according to

$$\begin{cases} p = p^*/P_0 & \boldsymbol{u} = \boldsymbol{u}^*/a_0 & r = r^*/R & T = T^*/T_0 \\ \rho = \rho^*/\rho_0 & t = t^*/(R/a_0) & z = z^*/R & \boldsymbol{\omega} = \boldsymbol{\omega}^*/(a_0/R) \end{cases} \tag{1}$$

where reference properties are defined in the Nomenclature. The normalized governing equations for a viscous compressible fluid, with no body forces acting on it, may be expressed as follows.

Mass:

$$\frac{\partial \rho}{\partial t} + \nabla \cdot (\rho \boldsymbol{u}) = 0 \tag{2}$$

Momentum:

$$\rho\left[\frac{\partial \boldsymbol{u}}{\partial t} + \frac{1}{2}\nabla(\boldsymbol{u}\cdot\boldsymbol{u}) - \boldsymbol{u}\times\nabla\times\boldsymbol{u}\right] = -\frac{1}{\gamma}\nabla p - \delta^2\nabla\times(\nabla\times\boldsymbol{u}) + \delta_d^2\nabla(\nabla\cdot\boldsymbol{u}) \tag{3}$$

Energy:

$$\rho\left(\frac{\partial T}{\partial t} + \boldsymbol{u}\cdot\nabla T\right) = \frac{\gamma-1}{\gamma}\left(\frac{\partial p}{\partial t} + \boldsymbol{u}\cdot\nabla p\right) + \frac{\delta^2}{Pr_0}\nabla^2 T \tag{4}$$

State:

$$p = \rho T \tag{5}$$

where Pr is the Prandtl number, γ is the ratio of specific heats, and the viscous parameters δ and δ_d are given by

$$\delta = \sqrt{\frac{\nu_0}{a_0 R}} = \sqrt{\frac{1}{Re_a}}; \qquad \delta_d = \delta\sqrt{\frac{\eta_0}{\mu_0} + \frac{4}{3}} \tag{6}$$

The next steps involve a decomposition of the flow variables in terms of mean flow and oscillatory components, followed by the expansion of all unsteady terms with respect to the primary perturbation parameter ε. As shown by Chu and Kovásznay [31], the variables can be split using

$$\boldsymbol{u} = M_b\boldsymbol{U} + \boldsymbol{u}'; \qquad \boldsymbol{\omega} = \bar{\boldsymbol{\Omega}} + \boldsymbol{\omega}'; \qquad p = 1 + p' \qquad \rho = 1 + \rho'; \qquad T = 1 + T' \tag{7}$$

Each fluctuating term may then be written as

$$a' = \varepsilon a^{(1)} + \varepsilon^2 a^{(2)} + \varepsilon^3 a^{(3)} + \mathcal{O}(\varepsilon^4) \tag{8}$$

Here, a alludes to a generic flow variable, and ε denotes the ratio of the superimposed oscillatory pressure amplitude to the traditionally larger mean chamber pressure. The last step consists of collecting the

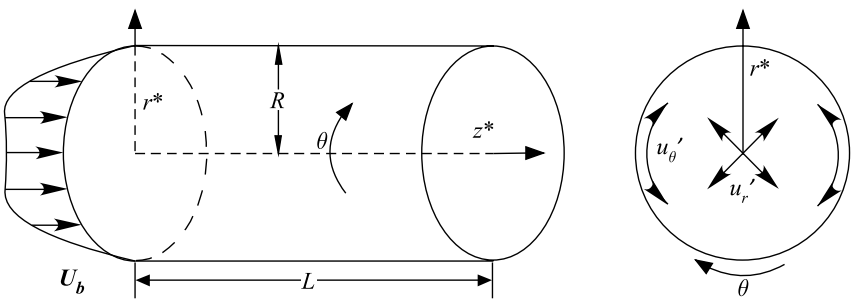

Fig. 1 Chamber geometry and coordinate system showing an axisymmetric profile. Also shown is a front view depicting the coupled tangential and radial (i.e., transverse) wave motions.

first-order fluctuations and separating them into acoustic and vortical fields [32,33]. As a result, the acoustic part gives rise to a compressible and inviscid motion, while the vortical part produces an incompressible but viscous field [34]. Using a circumflex to denote the pressure-driven potential part and a tilde for the boundary-driven vortical component, the unsteady flow variables may be once more decomposed into

$$a^{(1)} = \hat{a} + \tilde{a} \tag{9}$$

This step leads to two independent sets of equations that remain coupled by virtue of the no-slip requirement, which must be achieved along the boundaries [33]. These are as follows.

Acoustic set:

$$\begin{cases} \dfrac{\partial \hat{\rho}}{\partial t} = -\nabla \cdot \hat{\boldsymbol{u}} - M_b \boldsymbol{U} \cdot \nabla \hat{\rho} \\ \dfrac{\partial \hat{\boldsymbol{u}}}{\partial t} = -\dfrac{1}{\gamma} \nabla \hat{p} - M_b [\nabla (\boldsymbol{U} \cdot \hat{\boldsymbol{u}}) - \hat{\boldsymbol{u}} \times \bar{\boldsymbol{\Omega}}] \\ \hat{p} = \hat{T} + \hat{\rho} \\ \hat{p} = \gamma \hat{\rho} \end{cases} \tag{10}$$

and vortical set:

$$\begin{cases} \nabla \cdot \tilde{\boldsymbol{u}} = 0 \\ \dfrac{\partial \tilde{\boldsymbol{u}}}{\partial t} = -\dfrac{1}{\gamma} \nabla \tilde{p} - M_b [\nabla (\boldsymbol{U} \cdot \tilde{\boldsymbol{u}}) - \boldsymbol{U} \times \tilde{\boldsymbol{\omega}} - \tilde{\boldsymbol{u}} \times \bar{\boldsymbol{\Omega}}] - \delta^2 \nabla \times \tilde{\boldsymbol{\omega}} \\ \qquad + \delta_d^2 \nabla (\nabla \cdot \tilde{\boldsymbol{u}}) \end{cases} \tag{11}$$

C. Boundary Conditions

The acoustic and vortical fields require the use of two dissimilar sets of boundary conditions. In the case of an acoustic wave, a closed boundary must be maintained, as usual, along all solid surfaces, including the injection site (i.e., at $r = 1, z = 0$, and $z = L/R$). In the case of a rotational wave, the satisfaction of the no-slip condition at the headwall is usually of primary importance, being the counterpart of the sidewall boundary in the inverted analog of an axially traveling wave within an elongated porous cylinder [28,33]. In both geometric configurations, the velocity adherence constraint is imposed at the injecting surfaces, and these correspond to either the headwall or the sidewall of the simulated LRE and SRM, respectively. However, because the vortical waves driven by the injecting surfaces are determined in previous studies [28–30], slippage along the noninjecting surface (sidewall) must not be allowed in an improved formulation. Consistent with other boundary-layer studies, attenuation of the unsteady vorticity component is expected away from the sidewall. Therefore, at the centerline, the vorticoacoustic wave must reduce to its potential form. A summary of the physical constraints entailed in the resulting model is given in Table 1.

III. Solution

This section focuses on the boundary-layer approach that we follow to reduce the time-dependent vortical system into a more manageable set. The ensuing formulations are provided for axisymmetric mean flow profiles. However, before tackling the vortical set, it is helpful to resolve the acoustic wave first.

A. Acoustic Formulation

Although Eq. (10) consists of an assortment of four equations, these can be systematically reduced to a single PDE, which represents a modified form of the wave equation. By subtracting the derivative of the acoustic mass conservation from the divergence of the momentum equation, an extended form of the wave equation [28] may be readily revealed, specifically

$$\frac{\partial^2 \hat{p}}{\partial t^2} = \nabla^2 \hat{p} + M_b [\gamma \nabla^2 (\boldsymbol{U} \cdot \hat{\boldsymbol{u}}) - \gamma \nabla \cdot (\hat{\boldsymbol{u}} \times \bar{\boldsymbol{\Omega}}) - \frac{\partial}{\partial t} (\boldsymbol{U} \cdot \nabla \hat{p})] \tag{12}$$

Several detailed solutions of Eq. (12) are widely available in the literature. Here, we employ a solution that suitably describes the acoustic motion in a simulated LRE, where transverse waves dominate over their longitudinal counterparts. In this case, the complete leading-order acoustic field may be reproduced from

$$\hat{p} = e^{-ik_{mn}t} J_m(k_{mn} r) \cos(m\theta) \tag{13}$$

$$\hat{u}_r = \frac{i}{k_{mn}\gamma} e^{-ik_{mn}t} J_m'(k_{mn} r) \cos(m\theta) \tag{14}$$

$$\hat{u}_\theta = \frac{i}{k_{mn}\gamma} \frac{m}{r} e^{-ik_{mn}t} J_m(k_{mn} r) \sin(m\theta) \tag{15}$$

$$\hat{u}_z = 0 \tag{16}$$

where m and n are positive integers that refer to the tangential and radial mode numbers, respectively. In the same vein, k_{mn} designates the transverse wave number, where the numerical values of k_{mn} may be extracted from $J'(k_{mn}) = 0$. Equation (17) enumerates the roots of k_{mn} for the first eight wave numbers:

$$\begin{cases} k_{01} \approx 3.83170597 & k_{10} \approx 1.84118378 & k_{11} \approx 5.33144277 \\ k_{02} \approx 7.01558667 & k_{20} \approx 3.05423693 & k_{22} \approx 9.96946782 \\ k_{12} \approx 8.53631637 & k_{21} \approx 6.70613319 & \text{etc.} \end{cases} \tag{17}$$

In the interest of clarity, the four parts of Fig. 2 are intended to illustrate the instantaneous pressure distribution in a cylindrical chamber using four sequential mode numbers. These correspond to four zeroes of $J'(k_{mn})$ listed in Eq. (17). Everywhere, the pressure contours represent snapshots taken in a polar plane at $t = 0$ s, $\forall\ z$, where red and blue colors denote positive and negative acoustic pressures, respectively. It is interesting to note the evolution of the nodal lines going from Figs. 2a–2d, thus giving rise to double-D and alternating cross patterns that characterize the acoustic mode shapes. In Figs. 2a and 2b, the first and second radial modes are featured along with the first tangential mode where alternating double-D contours appear either a) once or b) twice, with the second set brushing along the outer periphery. In Figs. 2c and 2d, the second tangential configuration is depicted at the first and second radial modes. The last contour clearly captures the symmetrically alternating wave structure in both tangential and radial directions.

B. Vortical Formulation

Before proceeding with the formulation of the vortical wave structure, it may be useful to clarify the origin of the driving mechanisms for the waves in question. To this end, we recall that the acoustic waves are induced by pressure gradients within the chamber, and these remain immune to the effects of the no-slip requirement at the boundaries. They also display no sensitivity to the mean flow when taken at the leading order in M_b. In contrast, the traveling vortical waves are generated by the acoustic motion due to the presence of solid boundaries. They appear as a necessary correction that depends on the geometry at hand, the mean flow, and the acoustic

Table 1 Boundary conditions for the acoustic and vortical fields

	Boundary			
	$r = 0$	$r = 1$	$z = 0$	$z = L/R$
Acoustic field	No condition imposed	$\boldsymbol{n} \cdot \nabla \hat{p} = 0$	$\boldsymbol{n} \cdot \nabla \hat{p} = 0$	$\boldsymbol{n} \cdot \nabla \hat{p} = 0$
Vortical field	$\tilde{u}_r = \tilde{u}_\theta = \tilde{u}_z = 0$	$u_r' = u_\theta' = u_z' = 0$	No condition imposed	No condition imposed

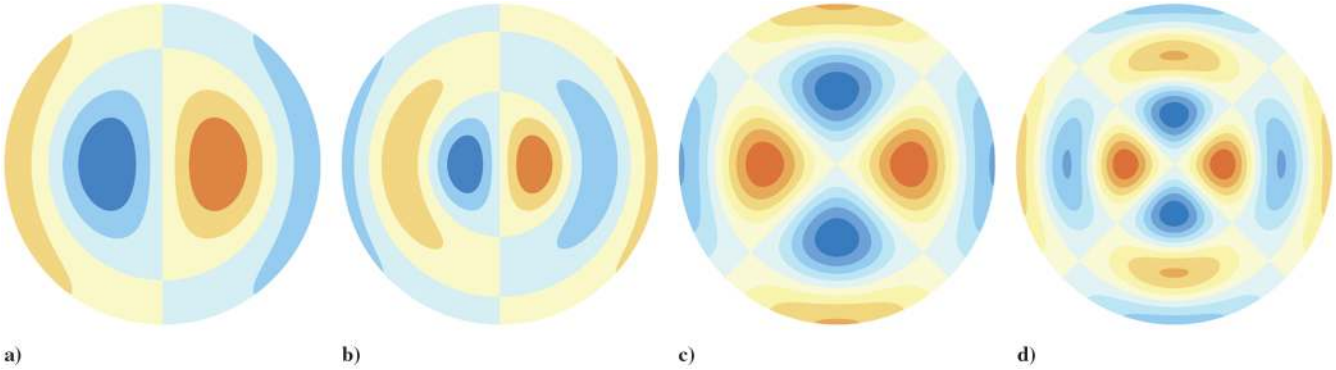

Fig. 2 Pressure contours in a polar slice for transverse oscillations corresponding to a) k_{11}, b) k_{12}, c) k_{21}, and d) k_{22}.

mode shapes. From this perspective, it may be argued that the vortical pressure distribution may be dismissed, and this may be attributed to the pressure differential being mainly prescribed by the acoustic field [13]. The foregoing assumption will be useful while solving for the vortical disturbance. However, at this stage, we find it necessary to retain the small vortical pressure wave $\tilde{p}$ in the momentum equation as we put

$$\nabla \cdot \tilde{\boldsymbol{u}} = 0 \tag{18}$$

$$\frac{\partial \tilde{\boldsymbol{u}}}{\partial t} = -\frac{1}{\gamma}\nabla \tilde{p} - M_b[\nabla(\boldsymbol{U}\cdot\tilde{\boldsymbol{u}}) - \boldsymbol{U}\times\tilde{\boldsymbol{\omega}} - \tilde{\boldsymbol{u}}\times\bar{\boldsymbol{\Omega}}] - \delta^2\nabla\times\tilde{\boldsymbol{\omega}} \tag{19}$$

In seeking an ansatz for $\tilde{\boldsymbol{u}}$, we note that, in Eqs. (18) and (19), the rotational velocity disturbance stands as a function of time and three spatial variables. Moreover, it is necessary to choose $\tilde{\boldsymbol{u}}(t, r, \theta, z)$ in a manner to offset the acoustic motion at the headwall, $\forall\ t$. The time dependence of the vortical field will then match that of the acoustic motion in the injection plane. This can be achieved when the unsteady vortical wave exhibits the form

$$\tilde{\boldsymbol{u}} = e^{-ik_{mn}t} f(r, \theta, z)$$
$$\text{or}\quad \frac{\partial \tilde{\boldsymbol{u}}}{\partial t} = -ik_{mn}e^{-ik_{mn}t} f(r, \theta, z) = -ik_{mn}\tilde{\boldsymbol{u}} \tag{20}$$

This particular ansatz will be used to secure a closed-form vortical approximation.

C. Boundary-Layer Approach

In-depth formulations that focus on wave characterization are presented by Haddad and Majdalani [29,30], where detailed solutions for axisymmetric injection profiles are constructed. In both studies, the vortical wave is generated at the headwall and propagates downstream. The present approach applies a similar perturbation expansion to a well-established variant of the conservation equations with the aim of capturing the development of the vortical wave at the sidewall. For the case of axisymmetric mean flows, Eqs. (18) and (19) may be expanded to produce

$$\frac{\tilde{u}_r}{r} + \frac{\partial \tilde{u}_r}{\partial r} + \frac{1}{r}\frac{\partial \tilde{u}_\theta}{\partial \theta} + \frac{\partial \tilde{u}_z}{\partial z} = 0 \tag{21}$$

$$-ik_{mn}\tilde{u}_r + M_b F\frac{\partial \tilde{u}_r}{\partial z} = -\frac{1}{\gamma}\frac{\partial \tilde{p}}{\partial r} + \delta^2\left(\frac{\partial^2 \tilde{u}_r}{\partial z^2} + \frac{1}{r^2}\frac{\partial^2 \tilde{u}_r}{\partial \theta^2} - \frac{1}{r^2}\frac{\partial \tilde{u}_\theta}{\partial \theta} - \frac{1}{r}\frac{\partial^2 \tilde{u}_\theta}{\partial r \partial \theta} - \frac{\partial^2 \tilde{u}_z}{\partial r \partial z}\right) \tag{22}$$

$$-ik_{mn}\tilde{u}_\theta + M_b F\frac{\partial \tilde{u}_\theta}{\partial z} = -\frac{1}{\gamma r}\frac{\partial \tilde{p}}{\partial \theta} + \delta^2\left(\frac{1}{r^2}\frac{\partial \tilde{u}_r}{\partial \theta} - \frac{1}{r}\frac{\partial^2 \tilde{u}_r}{\partial r \partial \theta} - \frac{\tilde{u}_\theta}{r^2} + \frac{\partial^2 \tilde{u}_\theta}{\partial z^2} + \frac{1}{r}\frac{\partial \tilde{u}_\theta}{\partial r} + \frac{\partial^2 \tilde{u}_\theta}{\partial r^2} - \frac{1}{r}\frac{\partial^2 \tilde{u}_z}{\partial \theta \partial z}\right) \tag{23}$$

$$-ik_{mn}\tilde{u}_z + M_b F\frac{\partial \tilde{u}_z}{\partial z} - M_b\frac{\partial F}{\partial r}\tilde{u}_r = -\frac{1}{\gamma}\frac{\partial \tilde{p}}{\partial z} + \delta^2\left(-\frac{1}{r}\frac{\partial \tilde{u}_r}{\partial z} - \frac{\partial^2 \tilde{u}_r}{\partial r \partial z} - \frac{1}{r}\frac{\partial^2 \tilde{u}_\theta}{\partial \theta \partial z} + \frac{1}{r^2}\frac{\partial^2 \tilde{u}_z}{\partial \theta^2} + \frac{1}{r}\frac{\partial \tilde{u}_z}{\partial r} + \frac{\partial^2 \tilde{u}_z}{\partial r^2}\right) \tag{24}$$

Recognizing that the vortical wave is most noticeable near solid surfaces, Eqs. (21–24) may be transformed using boundary-layer theory, with the no-slip boundary condition being enforced at the sidewall. Because the vortical wave can grow or decay in the radial direction, it is helpful to rescale the radial variable using a stretched inner coordinate of the form

$$\xi = \frac{1 - r}{\delta} \tag{25}$$

This spatial magnification is necessary because the near-wall boundary-layer correction cannot be captured when using the original variable r. Rescaling the radial coordinate serves a purpose similar to zooming onto the near wall region; only then would the inner behavior of the solution be revealed. The outer inviscid solution remains adequate except in the boundary-layer region, where viscous forces dominate. Moreover, being the inverted square root of the acoustic Reynolds number, the viscous parameter $\delta << 1$ can be suitably employed as a perturbation parameter. On this note, our subsequent step consists of expanding the vortical variables that appear in Eqs. (21–24) with respect to the viscous parameter. This can be accomplished using

$$\tilde{a} = \tilde{a}^{(0)} + \delta\tilde{a}^{(1)} + \delta^2\tilde{a}^{(2)} + \delta^3\tilde{a}^{(3)} + \mathcal{O}(\delta^4) \tag{26}$$

The process of collecting terms of the same order in δ and rearranging leads to a vortical set that must be solved to determine the leading order viscous correction. In doing so, caution must be exercised in handling terms of order M_b/δ. Because the Mach number and viscous parameters can appear at about the same order, their ratio can be of order unity and, hence, nonnegligible. At $\mathcal{O}(1)$, Eqs. (21–24) yield

$$\frac{\partial \tilde{u}_r^{(0)}}{\partial \xi} = 0 \tag{27}$$

$$\frac{\partial \tilde{p}^{(0)}}{\partial \xi} = 0 \tag{28}$$

$$ik_{mn}\tilde{u}_\theta^{(0)} + \frac{\partial^2 \tilde{u}_\theta^{(0)}}{\partial \xi^2} = \frac{1}{\gamma}\frac{\partial \tilde{p}^{(0)}}{\partial \theta} \tag{29}$$

$$ik_{mn}\tilde{u}_z^{(0)} + \frac{\partial^2 \tilde{u}_z^{(0)}}{\partial \xi^2} = \frac{1}{\gamma}\frac{\partial \tilde{p}^{(0)}}{\partial z} \tag{30}$$

Clearly, Eqs. (27–30) appear to be nearly decoupled, with the exception of the vortical pressure term appearing on the right-hand side of both the tangential and axial equations. Solving Eq. (28) yields a radially invariant $\tilde{p}^{(0)} = \tilde{p}^{(0)}(t,\theta,z)$. By analogy to the headwall correction at this order, the no-slip condition at the sidewall may be viewed as the main driver behind the bulk radial propagation of the vortical wave. The vortical pressure remains immaterial to the wave generated and can be set equal to zero. We therefore take

$$\tilde{p}^{(0)} = 0 \tag{31}$$

Forthwith, solving Eq. (27) leads to a radially invariant $\tilde{u}_r^{(0)}$ that must be suppressed to satisfy the no-slip condition at the sidewall. The value of $\tilde{u}_r^{(0)}$ can hence be deduced as

$$\tilde{u}_r^{(0)} = 0 \tag{32}$$

Now that $\tilde{p}^{(0)}$ has been settled, Eqs. (29) and (30) can be collapsed into a single equation. The general solution of the resulting ordinary differential equation (ODE) proves to be identical for both velocities. The differences emerge when applying the boundary conditions corresponding to each vortical component. For example, either axial or tangential equations reduce to

$$ik_{mn}\tilde{u}_{\theta,z}^{(0)} + \frac{\partial^2 \tilde{u}_{\theta,z}^{(0)}}{\partial \xi^2} = 0 \tag{33}$$

Equation (33) precipitates

$$\tilde{u}_{\theta,z}^{(0)} = A_{\theta,z}^{(0)}(t,\theta,z)e^{\phi_{mn}(r-1)} + B_{\theta,z}^{(0)}(t,\theta,z)e^{\phi_{mn}(1-r)} \tag{34}$$

where the radial parameter ϕ_{mn} depends on the acoustic mode and Reynolds numbers according to

$$\phi_{mn} = \frac{\sqrt{-ik_{mn}}}{\delta} \tag{35}$$

By ensuring that the vortical wave vanishes at the centerline, Eq. (34) becomes

$$\tilde{u}_{\theta,z}^{(0)} = A_{\theta,z}^{(0)}(t,\theta,z)[e^{-\phi_{mn}(1-r)} - e^{-\phi_{mn}(1+r)}] \tag{36}$$

Finally, the velocity adherence condition at the sidewall can be applied to each velocity component separately. This enables us to fully determine the axial and tangential components, namely

$$\tilde{u}_\theta^{(0)} = -\frac{im}{k_{mn}\gamma}J_m(k_{mn})\left[\frac{e^{-\phi_{mn}(1-r)} - e^{-\phi_{mn}(1+r)}}{1 - e^{-2\phi_{mn}}}\right]e^{-ik_{mn}t}\sin(m\theta) \tag{37}$$

$$\tilde{u}_z^{(0)} = 0$$

IV. Results and Discussion

The analytical approximations obtained heretofore can be collected into one set of expressions for the vorticoacoustic velocity and pressure distributions. It is worth noting that, at leading order, the vortical wave generated at the sidewall provides a correction for just the tangential component of the acoustic field. An evaluation of the remaining velocity components show that the latter vanish at $r \to 1$. Therefore, the following section focuses on the significance of the tangential correction and its properties.

To start, a summary of the vorticoacoustic wave components is provided by superimposing both potential and rotational contributions. The resulting unsteady disturbances may be presented as

$$p' = e^{-ik_{mn}t}J_m(k_{mn}r)\cos(m\theta) + \mathcal{O}(M_b,\delta) \tag{39}$$

$$u_r' = -\frac{i}{k_{mn}\gamma}e^{-ik_{mn}t}J_m'(k_{mn}r)\cos(m\theta) + \mathcal{O}(M_b,\delta) \tag{40}$$

$$u_\theta' = \frac{im}{k_{mn}\gamma}\left[\frac{J_m(k_{mn}r)}{rJ_m(k_{mn})} - \frac{e^{-\phi_{mn}(1-r)} - e^{-\phi_{mn}(1+r)}}{1 - e^{-2\phi_{mn}}}\right] \times e^{-ik_{mn}t}J_m(k_{mn})\sin(m\theta) + \mathcal{O}(M_b,\delta) \tag{41}$$

$$u_z' = 0 + \mathcal{O}(\delta) \tag{42}$$

For the sake of illustration, Fig. 3 is used to compare the behavior of the tangential disturbances for the strictly acoustic and its vorticoacoustic counterpart versus the radial coordinate at decreasing values of the viscous parameter. This is achieved at $t = 0.1$, $r = 0.4$, $\theta = \frac{1}{3}\pi$, $M_b = 0.03$, and a thrust chamber with a unit aspect ratio [28]. The corresponding plots capture the oscillatory motion for the first tangential with first radial modes using k_{11}.

A. Numerical Verification

By way of verification, a numerical solver is written to compute the solution corresponding to Eq. (33). The solver uses a shooting scheme in conjunction with Mathematica's built-in numerical integrators to perform the necessary calculations. To ensure numerical stability and reduce interpolation errors, we find it essential to begin integrating at the end of the domain, where $r = 1$, and work our way backward to the centerline.

To ensure conformity between the derived analytical solutions and their numerical counterparts, we evaluate the tangential vortical equation for the cases described in the previous section. The numerical results are shown using dash-dots in Fig. 3. Given that the level of agreement between numerics and asymptotics is favorable, we now proceed to characterize the vorticoacoustic wave based on the analytical solution given by Eq. (41).

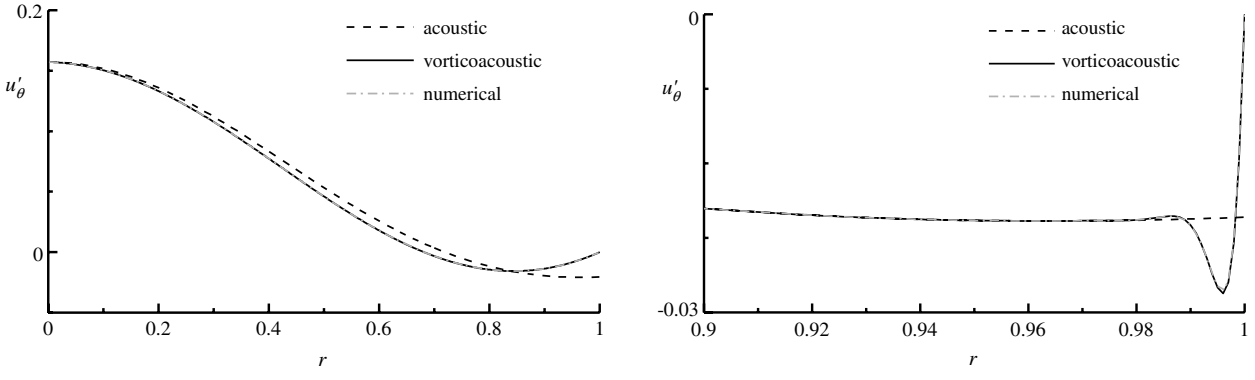

Fig. 3 Acoustic and vorticoacoustic tangential velocities at k_{11} and δ corresponding to a) 0.5, and b) 0.005.

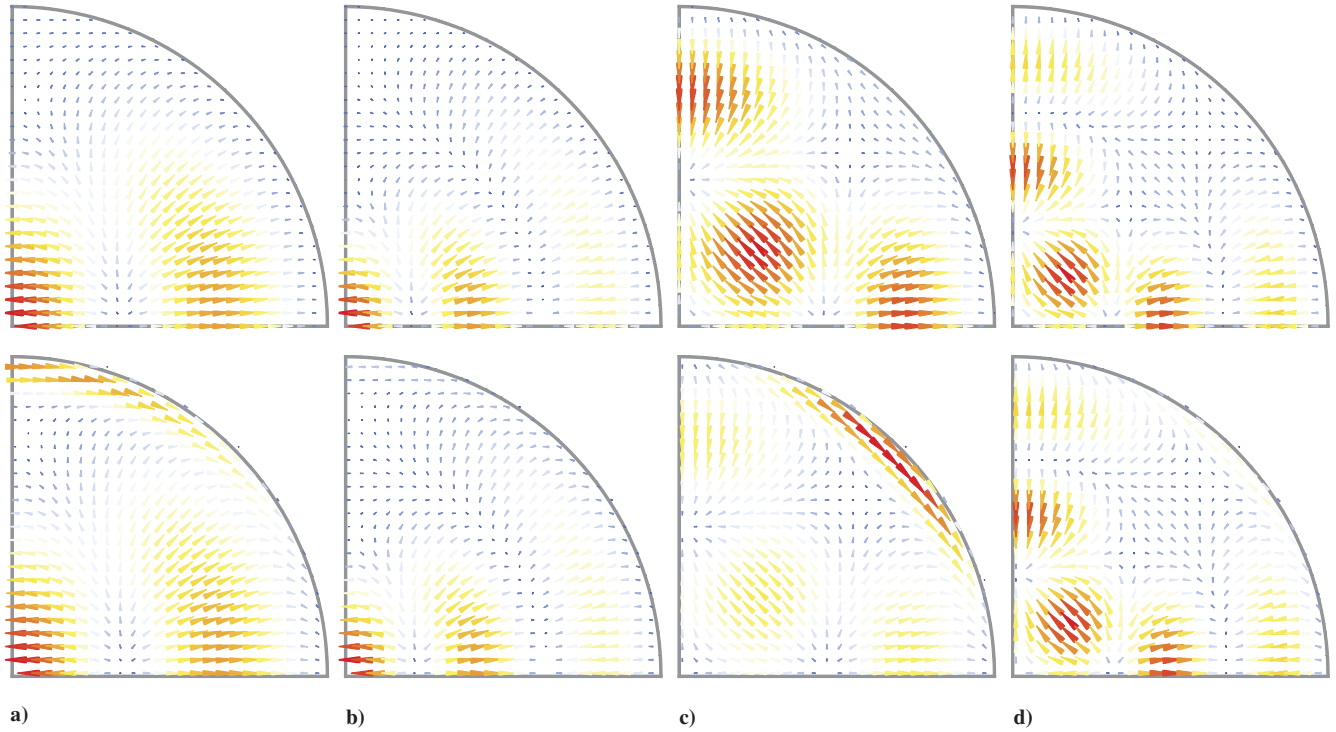

Fig. 4 Unsteady velocity vectors in the first polar quadrant for the acoustic (top row) and vorticoacoustic oscillations (bottom) corresponding to a) k_{11}, b) k_{12}, c) k_{21}, and d) k_{22}.

B. Wave Characterization

A fundamental distinction differentiates the sidewall boundary layer from its headwall counterpart: its independence from the injection Mach number and showerhead patterns. At leading order, this behavior may be attributed to the dissimilar forms of the dissipation mechanisms occurring near each boundary. Because the bulk streamwise motion of the fluid remains axial, a contribution of the injection mechanism is expected to be significant (and is therefore captured) in the leading-order solution [30]. In contrast, the radial direction represents a secondary axis with respect to the mean flow motion. It then follows that the bulk development of the boundary layer at the sidewall remains unaffected by the mean flow at leading order. Such contributions are expected to start appearing at $\mathcal{O}(\delta^2)$ and higher.

Figure 3 illustrates the dependence of the wave's boundary-layer thickness on the viscous parameter. It is apparent that viscous forces dominate over inertial forces as the viscous parameter is increased. Conversely, when the latter is reduced, the boundary layer diminishes in the vicinity of the sidewall region. This behavior is consistent with the predictions of classical boundary-layer theory, namely of an increased boundary-layer thickness with successive increases in δ or, alternatively, decreases in the Reynolds number [34].

It should be noted that, in some cases, the satisfaction of the no-slip requirement at a solid boundary induces an abrupt change in the outer (acoustic) flow. This change manifests itself in an overshoot taking place in the near-wall region [30,34]. As usual, the phase shift between the vortical and acoustic fields leads to a positive coupling of the tangential velocity. This behavior is illustrated in Figs. 3b and 4. The latter showcases the velocity vectors resulting from the pressure fields in Fig. 2. In Fig. 4, the top part represents the transverse acoustic velocities in the first quadrant, while the bottom part features the vorticoacoustic fields at $\delta = 0.1$. It may be worth noting that, near the wall, the vorticoacoustic velocities display a sharp tangential peak before depreciating to zero at the sidewall, in fulfillment of the no-slip requirement at $r = 1$.

C. Radial Penetration Number

The behavior of vortical waves usually depends on a multitude of flow parameters such as the injection Mach number, the viscous parameter, and acoustic parameters such as the Strouhal and wave numbers. In studies pertaining to vorticoacoustic waves in SRMs [34] and LREs [30], these parameters are shown to collapse into the Strouhal and penetration numbers, which strongly control the frequency and magnitude of the waves, respectively.

Along similar lines, a close examination of Eqs. (35–37) enables us to infer that the behavior of the tangential waves depends on a combination of the mode number k_{mn} and the viscous parameter δ. In fact, the expression for the radial control parameter may be written as

$$\phi_{mn} = \sqrt{\frac{-i}{S_r}}$$

where $S_r = \delta^2/k_{mn}$ represents the radial penetration number.

Figure 5 depicts the radial distribution of the vortical wave for different values of the control parameters. This graph also confirms the importance of the penetration number in prescribing the magnitude of the viscous boundary layer generated at the sidewall. On one hand, Fig. 5a shows that, given a fixed acoustic wave number of k_{11}, successive reductions in the radial penetration number (or viscosity) lead to corresponding decrements in the rotational depth of penetration. This result confirms the observations in Fig. 3a, wherein a viscous parameter of 0.5 can be seen to produce a wave that is almost swept through the entirety of the chamber; conversely, a value of 0.005 in Fig. 3b leads to a wave decaying rapidly in the vicinity of the sidewall.

On the other hand, Fig. 5b shows that the depth of penetration (i.e., the size of the boundary-layer thickness) depends solely on the radial penetration number. When fixed to a certain value such as 1000 in the case of Fig. 5b, the vortical wave decays at the same location irrespective of the particular values of k_{mn} and δ. Physically, a constant value of the penetration number ensures that the increase in the amount of friction between shear layers due to faster rates of flow reversals at higher frequencies is offset by a decrease in viscosity. The overall fixed attenuation level proves to be a byproduct of both mechanisms whose relative importance dictates the value of S_r and, consequently, the radial boundary-layer thickness δ_{BL}. Therefore, the radial penetration number can be seen as a measure of the relative

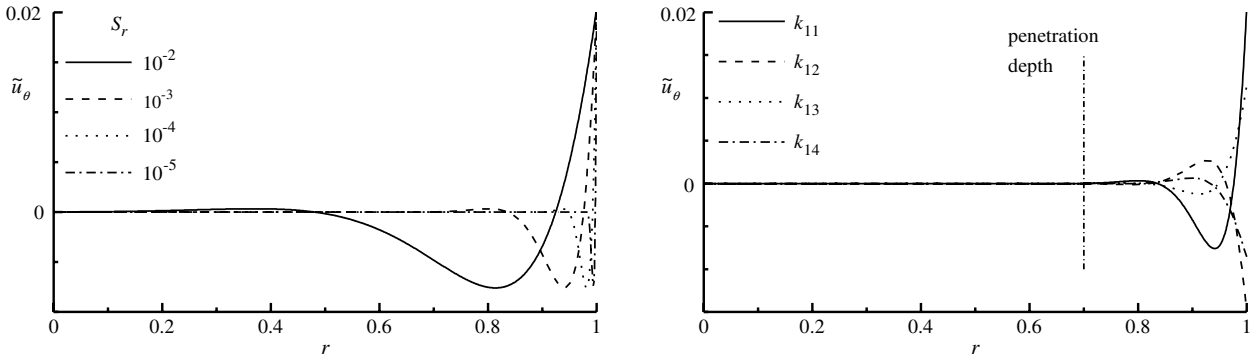

Fig. 5 Behavior of tangential vortical wave for a) $k_{11} = 5.3314$, and b) $S_r = 1000$.

importance of viscous and unsteady forces. In this study, we find δ_{BL} to be proportional to the penetration number, or

$$\delta_{\mathrm{BL}} \approx S_r = \frac{1}{k_{mn} Re_a} = \frac{1}{k_{mn}} \frac{\nu_0}{a_0 R} = \left(\frac{a_0}{\omega_{mn} R}\right)\left(\frac{\nu_0}{a_0 R}\right) = \left(\frac{\sqrt{\nu_0/\omega_{mn}}}{R}\right)^2 = \frac{1}{Re_k} \tag{44}$$

where ω_{mn} is the circular frequency associated with a given transverse mode number. Clearly, the radial penetration number scales with the ratio of the Stokes layer $\sqrt{2\nu_0/\omega_{mn}}$ and the characteristic length R. Furthermore, it proves to be identical to the reciprocal of the kinetic Reynolds number Re_k. Using the transverse frequency as a basis, S_r may be connected to the Womersley number, $\alpha = R\sqrt{\omega_{mn}/\nu_0}$, or the Stokes number, $\lambda_S = R\sqrt{\omega_{mn}/(2\nu_0)}$, via

$$S_r = \frac{1}{2}\left(\frac{\sqrt{2\nu_0/\omega_{mn}}}{R}\right)^2 = \frac{1}{2\lambda_S^2} = \frac{1}{\alpha^2} \tag{45}$$

This result is somewhat reassuring, given the relevance of the Stokes and Womersley numbers to oscillatory motions over nontranspiring surfaces.

V. Conclusions

In this study, asymptotic expansion tools are used to capture small-amplitude oscillations that are dominated by their transverse motion in short cylindrical chambers that mimic the cold-flow environment of a simple liquid rocket engine. After decomposing the unsteady wave into potential and rotational fields, the latter is resolved using a boundary-layer formulation that depends in large part on a small viscous parameter δ. At the outset, several fundamental flow characteristics of the tangential component of motion are evaluated and described. As before, the pseudopressure associated with the rotational motion is determined systematically and shown to be immaterial to the present analysis. The radial penetration number, a fundamental parameter that controls the depth of penetration of unsteady vorticity, is clearly identified. Its connection to the Stokes or Womersley numbers is also affirmed. The advent of this parameter enables us to fully characterize the depth of penetration in the radial direction.

With the vorticoacoustic solution at hand, the velocity distributions in different polar cross sections are carefully examined. These are found to be strongly dependent on the radial penetration number, which combines the transverse wave number and the viscous parameter $S_r = \delta^2/k_{mn} = \frac{1}{2}\lambda_S^{-2}$. The latter, though different from its axial counterpart, represents an essential parameter that recurs whenever oscillatory wave motion is considered near a solid boundary with or without surface transpiration. In future work, a combination of sidewall and headwall corrections will be considered with the aim of providing a complete representation of the vortical field in a liquid rocket engine. It is also hoped that a similar mathematical strategy will be pursued to achieve asymptotically accurate models of vorticoacoustic waves in various physical settings.

Acknowledgments

This material is based on work supported partly by the National Science Foundation and, partly, by the H. H. Arnold Chair of Excellence in Advanced Propulsion at the University of Tennessee Space Institute.

References

[1] Hart, R., and McClure, F., "Combustion Instability: Acoustic Interaction with a Burning Propellant Surface," *Journal of Chemical Physics*, Vol. 30, No. 6, 1959, pp. 1501–1514. doi:10.1063/1.1730226

[2] Hart, R., and McClure, F., "Theory of Acoustic Instability in Solid-Propellant Rocket Combustion," *Proceedings of the 10th Symposium (International) on Combustion*, Vol. 10, Combustion Inst., Pittsburgh, PA, 1965, pp. 1047–1065.

[3] Culick, F., "Stability of High Frequency Pressure Oscillations in Rocket Combustion Chambers," *AIAA Journal*, Vol. 1, No. 5, 1963, pp. 1097–1104. doi:10.2514/3.1730

[4] Culick, F., "Acoustic Oscillations in Solid Propellant Rocket Chambers," *Acta Astronautica*, Vol. 12, No. 2, 1966, pp. 113–126. doi:10.1063/1.1730226

[5] Majdalani, J., Flandro, G., and Roh, T., "Convergence of Two Flowfield Models Predicting a Destabilizing Agent in Rocket Combustion," *Journal of Propulsion and Power*, Vol. 16, No. 3, 2000, pp. 492–497. doi:10.2514/2.5595

[6] Majdalani, J., "Vorticity Dynamics in Isobarically Closed Porous Channels. Part 1: Standard Perturbations," *Journal of Propulsion and Power*, Vol. 17, No. 2, 2001, pp. 355–362. doi:10.2514/2.5749

[7] Majdalani, J., and Roh, T., "Vorticity Dynamics in Isobarically Closed Porous Channels. Part 2: Space-Reductive Perturbations," *Journal of Propulsion and Power*, Vol. 17, No. 2, 2001, pp. 363–370. doi:10.2514/2.5750

[8] Brown, R. S., Blackner, A. M., Willoughby, P. G., and Dunlap, R., "Coupling Between Acoustic Velocity Oscillations and Solid Propellant Combustion," *Journal of Propulsion and Power*, Vol. 2, No. 5, 1986, pp. 428–437. doi:10.2514/3.22925

[9] Dunlap, R., Blackner, A., Waugh, R., Brown, R., and Willoughby, P., "Internal Flow Field Studies in a Simulated Cylindrical Port Rocket Chamber," *Journal of Propulsion and Power*, Vol. 6, No. 6, 1990, pp. 690–704. doi:10.2514/3.23274

[10] Vuillot, F., and Avalon, G., "Acoustic Boundary Layers in Large Solid Propellant Rocket Motors Using Navier–Stokes Equations," *Journal of Propulsion and Power*, Vol. 7, No. 2, 1991, pp. 231–239. doi:10.2514/3.23316

[11] Majdalani, J., and Van Moorhem, W., "Multiple-Scales Solution to the Acoustic Boundary Layer in Solid Rocket Motors," *Journal of Propulsion and Power*, Vol. 13, No. 2, 1997, pp. 186–193. doi:10.2514/2.5168

[12] Majdalani, J., and Van Moorhem, W., "Improved Time-Dependent Flowfield Solution for Solid Rocket Motors," *AIAA Journal*, Vol. 36, No. 2, 1998, pp. 241–248. doi:10.2514/2.7507

[13] Majdalani, J., and Roh, T., "The Oscillatory Channel Flow with Large Wall Injection," *Proceedings of the Royal Society of London, Series A*, Vol. 456, No. 1999, 2000, pp. 1625–1657. doi:10.1098/rspa.2000.0579

[14] Majdalani, J., and Flandro, G., "The Oscillatory Pipe Flow with Arbitrary Wall Injection," *Proceedings of the Royal Society of London, Series A*, Vol. 458, No. 2023, 2002, pp. 1621–1651. doi:10.1098/rspa.2001.0930

[15] Zhou, C., and Majdalani, J., "Improved Mean-Flow Solution for Slab Rocket Motors with Regressing Walls," *Journal of Propulsion and Power*, Vol. 18, No. 3, 2002, pp. 703–711. doi:10.2514/2.5987

[16] Xu, H., Lin, Z., Liao, S., Wu, J., and Majdalani, J., "Homotopy Based Solutions of the Navier–Stokes Equations for a Porous Channel with Orthogonally Moving Walls," *Physics of Fluids*, Vol. 22, No. 5, 2010, p. 053601. doi:10.1063/1.3392770

[17] Majdalani, J., Vyas, A., and Flandro, G., "Higher Mean-Flow Approximation for a Solid Rocket Motor with Radially Regressing Walls," *AIAA Journal*, Vol. 40, No. 9, 2002, pp. 1780–1788. doi:10.2514/2.1854

[18] Kurdyumov, V., "Steady Flows in the Slender, Noncircular, Combustion Chambers of Solid Propellants Rockets," *AIAA Journal*, Vol. 44, No. 12, 2006, pp. 2979–2986. doi:10.2514/1.21125

[19] Majdalani, J., "On Steady Rotational High Speed Flows: The Compressible Taylor–Culick Profile," *Proceedings of the Royal Society of London, Series A*, Vol. 463, No. 2077, 2007, pp. 131–162. doi:10.1098/rspa.2006.1755

[20] Chu, W., Yang, V., and Majdalani, J., "Premixed Flame Response to Acoustic Waves in a Porous-Walled Chamber with Surface Mass Injection," *Combustion and Flame*, Vol. 133, No. 3, 2003, pp. 359–370. doi:10.1016/S0010-2180(03)00018-X

[21] Chu, W.-W., Yang, V., Vyas, A. B., and Majdalani, J., "Premixed Flame Response to Acoustic Waves in a Porous-Walled Chamber with Surface Mass Injection," *38th AIAA/ASME/SAE/ASEE Joint Propulsion Conference and Exhibit*, AIAA Paper 2002-3609, July 2002.

[22] Majdalani, J., "The Oscillatory Channel Flow with Arbitrary Wall Injection," *Journal of Applied Mathematics and Physics (ZAMP)*, Vol. 52, No. 1, 2001, pp. 33–61. doi:10.1007/PL00001539

[23] Maslen, S., and Moore, F., "On Strong Transverse Waves Without Shocks in a Circular Cylinder," *Journal of the Aeronautical Sciences*, Vol. 23, No. 6, 1956, pp. 583–593. doi:10.2514/8.3612

[24] Crocco, L., Harrje, D. T., and Reardon, F. H., "Transverse Combustion Instability in Liquid Propellant Rocket Motors," *Journal of the American Rocket Society*, Vol. 32, 1962, p. 366.

[25] Zinn, B. T., and Savell, C. T., "A Theoretical Study of Three-Dimensional Combustion Instability in Liquid-Propellant Rocket Engines," *Proceedings of the 12th Symposium (International) on Combustion*, Vol. 12, Combustion Inst., Pittsburgh, PA, 1969, pp. 139–147.

[26] Flandro, G. A., Majdalani, J., and Sims, J. D., "Nonlinear Longitudinal Mode Instability in Liquid Propellant Rocket Engine Preburners," *40th AIAA/ASME/SAE/ASEE Joint Propulsion Conference and Exhibit*, AIAA Paper 2004-4162, July 2004.

[27] Flandro, G. A., Majdalani, J., and Sims, J. D., "On Nonlinear Combustion Instability in Liquid Propellant Rocket Engines," *40th AIAA/ASME/SAE/ASEE Joint Propulsion Conference and Exhibit*, AIAA Paper 2004-3516, July 2004.

[28] Fischbach, S., Flandro, G., and Majdalani, J., "Acoustic Streaming in Simplified Liquid Rocket Engines with Transverse Mode Oscillations," *Physics of Fluids*, Vol. 22, No. 6, 2010, p. 063602. doi:10.1063/1.3407663

[29] Haddad, C. T., and Majdalani, J., "Transverse Waves in Simulated Liquid Rocket Engines," *AIAA Journal*, Vol. 51, No. 3, 2013, pp. 591–605. doi:10.2514/1.J051912

[30] Haddad, C. T., and Majdalani, J., "Transverse Waves in Simulated Liquid Rocket Engines with Variable Headwall Injection," *50th AIAA Aerospace Sciences Meeting*, AIAA Paper 2012-0541, Jan. 2012.

[31] Chu, B.-T., and Kovásznay, L. S. G., "Non-Linear Interactions in a Viscous Heat-Conducting Compressible Gas," *Journal of Fluid Mechanics*, Vol. 3, No. 5, 1958, pp. 494–514. doi:10.1017/S0022112058000148

[32] Carrier, B. T., and Carlson, F. D., "On the Propagation of Small Disturbances in a Moving Compressible Fluid," *Quarterly of Applied Mathematics*, Vol. 4, No. 1, 1946, pp. 1–12.

[33] Majdalani, J., "Multiple Asymptotic Solutions for Axially Travelling Waves in Porous Channels," *Journal of Fluid Mechanics*, Vol. 636, 2009, pp. 59–89. doi:10.1017/S0022112009007939

[34] Majdalani, J., "The Boundary Layer Structure in Cylindrical Rocket Motors," *AIAA Journal*, Vol. 37, No. 4, 1999, pp. 505–508. doi:10.2514/2.742

T. Jackson
Associate Editor